Adjoint shape optimization coupled with LES-adapted RANS of a U-bend duct for pressure loss reduction

Computers and Fluids 228 (2021) 105057

Contents lists available at ScienceDirect

Computers and Fluids

journal homepage: www.elsevier.com/locate/compfluid

Adjoint shape optimization coupled with LES-adapted RANS of a U-bend duct for pressure loss reduction

G. Alessi [*,a,b], T. Verstraete [a], L. Koloszar [a], B. Blocken [c,b], J.P.A.J. van Beeck [a]

[a] von Karman Institute for Fluid Dynamics, Sint-Genesius-Rode B-1640, Belgium
[b] Department of Civil Engineering, KU Leuven, Heverlee 3001, Belgium
[c] Department of the Built Environment, Eindhoven University of Technology, Eindhoven 5600MB, The Netherlands

ARTICLE INFO

Keywords:
Adjoint shape optimization
RANS
LES
Cahotic flow motion
2010 MSC:
00-01
99-00

ABSTRACT

Nowadays, as industrial designs are close to their optimal configurations, the challenge lies in the extraction of the last percentages of improvement. This necessitates accurate evaluations of the performance and represents a significant higher computational cost. The present work aims at integrating Large Eddy Simulations in the optimization framework for an accurate evaluation of the flow field. The number of expensive evaluations is kept to a minimum by using the adjoint method for the evaluation of the gradient of the objective function. Divergence of the gradients due to the chaotic flow motion is avoided by an additional step which decouples the Large Eddy Simulations from the gradient calculations. An adaptation process based on a Reynolds Averaged Navier-Stokes simulation is therefore sought to mimic the more accurate Large Eddy Simulation results. The obtained field is then used in combination with an adjoint shape optimization routine. The method is tested on the design of a U-bend for internal cooling channels by minimizing its pressure loss. Starting from an optimized geometry obtained through a classical approach based on RANS evaluations, further improvements of the design are achieved with the application of the proposed strategy when performances are evaluated by means of LES.

1. Introduction

Product developments are nowadays assisted by computer software to speed-up the design process. Problems involving fluid dynamics can be simulated numerically, avoiding expensive experimental campaigns when many different design configurations need to be analyzed. This enables the use of computer aided optimization algorithms to search autonomously for design improvements. Usually the relationship between shape and its effect on performance is rather complex and beyond the capability of human designers to be accurately predicted, which is why design processes driven by human instincts are mainly characterised by a trial and error process. On the other hand, numerical shape optimization algorithms, especially when guided by gradient information, allow to obtain performance improvements in a few cycles adjusting the design. As such, optimization routines have gained sufficient maturity to be deployed in an industrial context in the design process [1,2], reducing significantly the design time and the number of experimental tests needed.

The accuracy of the optimization result largely depends on the numerical model used to simulate the flow. Reynolds Averaged Navier-Stokes (RANS) simulations are commonly used both in academia and industry due to the acceptable numerical cost [3–5]. This allows to explore a wide range of different configurations within the context of a design activity [1]. The prediction capability of RANS is however limited: highly three dimensional flows with secondary motions, flows with strong pressure gradients on the boundary layer, or flows with strong separations for instance are not well predicted by the steady state RANS approach and may guide the optimization algorithm to an erroneous optimal solution. More accuracy is possible by means of a Large Eddy Simulation (LES) approach, where large unsteady turbulent structures are resolved. However, due to larger spatial discretization requirements and because the simulation is time-resolved, the computational cost increases significantly compared to RANS. The role LES has within the design process was therefore initially quasi-similar to an experimental validation, and mainly performed in a final stage. But as computational power keeps increasing, LES within an optimization framework is becoming possible. As an example, Marsden et al. applied a gradient-free optimization in conjunction with LES to reduce the noise generated by turbulent flow over a hydrofoil trailing edge [6]. Goit and Meyer used LES with the aim of increasing the total energy extraction in wind farms [7]. Collis and Chang considered LES for determining the

* Corresponding author.
E-mail address: giacomo.alessi@vki.ac.be (G. Alessi).

https://doi.org/10.1016/j.compfluid.2021.105057
Received 8 March 2020; Received in revised form 27 May 2021; Accepted 21 June 2021
Available online 26 June 2021

Nomenclature

U	mean velocity
$\overline{U}$	mean velocity from LES
U_0	mean uniform inlet velocity
U^*	normalized mean velocity
p	mean static pressure
p^*	mean normalized static pressure
U_a	mean adjont velocity
q	mean adjoint pressure
$T.I.$	turbulence intensity
D_h	hydraulic diameter
V	cell volume
ϕ	mean face volumetric flux
ν	laminar viscosity
ν_t	turbulent viscosity
J	objective function
Ω	volume
Γ	boundaries
L	augmented objective function
$\mathbf{n}$	boundary normal
$\mathbf{x}$	coordinates
λ	step size
γ	relaxation factor
β	step size for the line search
S	surface sensitivity

optimal control of a turbulent flow for drag reduction problems [8].

Two main strategies exist when dealing with optimization problems. A first strategy requires only the evaluation of the objective function and does not need the computation of its gradient. Such optimization strategies are mainly non-deterministic and require in general a large amount of simulations to be performed to reach an optimum, while the degrees of freedom given to the design are rather limited. A second strategy is based on the calculation of the gradient of the objective function. This strategy gives to the optimizer a direct hint on how the design needs to be changed to reach a certain improvement. This leads to a more efficient algorithm, especially when the gradient is computed using the adjoint approach, with a cost nearly independent of the number of control variables. For this reason the application of gradient based optimization is very attractive within a LES context.

The adjoint method had been originally developed by Lions [9] in the context of control theory. The first application in the aerodynamics field goes back to Pironneau [10], who studied the energy dissipation due to a small hump on a body in a uniform steady flow with the aim to obtain the optimal condition for different drag minimization problems. Jameson introduced the technique in the aeronautical field [11] developing the adjoint counterpart of the Euler equations. The work of Jameson aimed to show how the design problem could be tackled through control theory, in which in particular the control is the shape of the boundary. The design problem considered was the search for an airfoil profile which gives a prescribed pressure distribution. The adjoint method continued to grow in the aeronautical industry framework bringing its use for: complete aircraft optimization [12], problems considering the compressible Navier-Stokes equations [13], aero-structural optimization [14,15]. The examples illustrated above are related to the aeronautical field but applications can be found in many other different domains, such as turbomachinery [16,17], automotive [18–20], energy [7], naval [21] and thermal exchange [22,23]. In the context of shape optimization, the coupling with deformation techniques [24,25] is necessary after the evaluation of the direction of improvement.

The application of gradient based optimization techniques using LES is however not widespread and it is so far mainly limited to control problems [7,8] with short time-averaging windows. The reason is that the adjoint method becomes unstable and diverges due to the ”butterfly effect” [26,27]. Due to the chaotic nature of the flow, small perturbations in flow quantities, whether they come from numerical round-off or from a perturbed mesh, will increase exponentially in time such that after a certain time the perturbed flow will be totally different from the unperturbed one. The objective function for an optimization is typically a time averaged flow quantity, and hence, for a limited averaging period, it may lead to a completely different objective function value for a slightly perturbed shape. This remains so for the linearized model and thus the sensitivities computed through the adjoint method become unreliable.

The use of LES within a gradient based optimization approach hence remains an active field of research. Many solutions have been proposed, of which the Least Square Shadowing Technique [28,29] is the most promising. This technique makes use of the shadowing lemma [30,31], which states that for each numerical trajectory in a chaotic dynamic system, a true trajectory can be found which is very close to the former one with slightly different initial conditions, even though the numerical trajectory would diverge exponentially from the true one if the same initial condition would be used. Applying this technique to LES, it implies that, when the grid is perturbed, a flow solution can be found near to the original one if a slightly different initial flow field would be used. As a consequence, the derivative of the objective function calculated is meaningful and can be used to drive the solution to its optimum. The Least Square Shadowing technique requires thus to find the initial flow field such that it shadows the original flow field time-evolution. This is an optimization problem with a very large set of degrees of freedom, which would significantly increase the overall computational cost. Some methods to reduce the cost of the optimization of the initial field have been proposed [32–34]. Nonetheless, to date the Least Square Shadowing Technique can only be applied to very small numerical domains, far below the current interest.

For this reason, another approach is chosen in the present work. Two observations lay at the basis of the proposed method: 1) RANS models fail to predict the time-averaged LES flow field mainly because of an inapt turbulence model, and 2) the gradients can in many cases be approximatively obtained using a frozen turbulence approach, which considers the turbulent viscosity invariant under small shape perturbations [35,36]. The novel approach presented here includes an initial step where a suitable RANS model is sought to fit the time-averaged flow field of the LES simulation. Hereto, the turbulent viscosity of each cell in the RANS simulation is adapted to yield a similar flow field as the LES result. This step requires an optimization and is similar to the work reported in Hayek et al. [37], in which a discrete adjoint formulation is presented. Once the RANS model is established, the adjoint method is used to compute the surface sensitivities under the assumption of constant turbulent viscosity. An optimizer allows then to update the shape, after which the full procedure is repeated. A new LES calculation is thus performed, followed by a RANS simulation adapting the turbulent viscosity, the computation of the adjoint field and of the surface sensitivities and, finally, the shape modification. The procedure is repeated until no significant improvement is further obtained. The proposed strategy allows to combine the reliability of a LES evaluation to a low computational cost optimization routine through the link with a RANS approach.

The method is applied to the optimization of a U-bend, being a prototype test case for which RANS is proven to be insufficiently reliable. The U-bend test case is described in Verstraete et al. and Coletti et al. [38,39] and optimized to reduce the pressure drop which arises from the significant flow turning [38]. A large reduction in pressure

drop was achieved by a classical RANS-based optimization algorithm through shape modifications that suppressed the flow separation in the bend. However, a recirculation bubble, not detected by the RANS evaluation, is still present inside the design as revealed by the experimental validation through Particle Image Velocimetry (PIV) [39]. On the other hand, simulations using LES could replicate with high accuracy the experimental findings [40]. To further improve the U-bend design, a LES based approach is thus inevitable.

The paper is structured as follows: first the U-bend test case will be described in more detail. A following section focuses on the LES-based optimization approach used. The subsequent section then applies the approach to the U-bend and finally some conclusions are drawn.

2. The U-bend test case

Gas turbines are cooled by internal flows with air which is usually bled from the compressor, leading to a loss in thermodynamic efficiency. The design of the internal cooling system can be improved by reducing the internal losses and thus reducing the amount of work needed from the compressor. The U-bends which connect the different coolant passages are significant contributors to the pressure losses inside the system [41]. As a consequence, they have been the subject of many optimization studies [17,42–45].

The starting point of the present work is the optimized design obtained in Verstraete et al. [38]. The initial design is represented by a circular U-bend of square section (hydraulic diameter $D_h = 0.075m$), Fig. 1a. The optimal shape, obtained by means of a metamodel assisted differential evolution algorithm, is shown in Fig. 1b. The numerical domain is completed by a $8D_h$ long straight channel connected to each side of the bend illustrated in Fig. 1. The domain is three dimensional but no variation to the shape is given in the z-direction.

This section presents the comparison of RANS, LES and experiments of the optimized geometry obtained in Verstraete et al. [38] and serves to validate the numerical set-up. As the experimental configuration has very long inlet and outlet legs for developing the velocity profile [38,39], the numerical domain is shortened to reduce the computational cost. The boundary conditions for the simulations are extrapolated from a RANS evaluation of the experimental configuration, sampling the velocity field and the turbulent quantities at the location corresponding to the inlet of the numerical configuration. A uniform inlet velocity, U_0=8.4 m/s, and a turbulence intensity $T.I. = 5\%$ are considered for the simulation of the experimental configuration, in analogy with the experimental campaign. Differently from the RANS simulations for which the aforementioned procedure is followed, a zero turbulence level is imposed at the inlet of the numerical configuration in the LES, as the bend itself trigger the turbulent structures. The Reynolds number is 40000. A zero static gauge pressure boundary condition is imposed at the outlet and a no-slip condition to the walls. The simulations, both RANS and LES, are performed using a structured grid with 342x50x50 cells with local refinements in the regions of high curvature and a maximum y^+ value of 2.2. A mesh convergence study is performed with finer meshes with a maximum y^+ value of 0.9; since no variation of the results is observed, the coarser mesh is used.

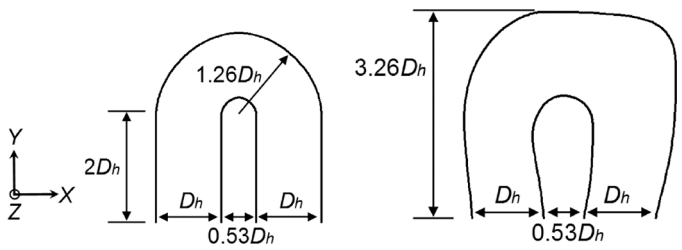

(a) Initial. (b) Optimized.

Fig. 1. U-bend geometries.

The RANS and LES simulations are carried out using the simpleFoam and pimpleFoam solver from OpenFOAM [46], respectively. The open-source CFD software OpenFOAM uses a finite-volume cell-centered approach in which the flow equations are solved in a segregated manner by means of the SIMPLE and PIMPLE algorithm, respectively for the RANS and LES approach. The turbulence model equations are solved separately. The Launder-Sharma low-Reynolds $k-\epsilon$ turbulence model is used in the RANS simulations. Although the model chosen is not expected to give extremely reliable results for high turbulent flow with swirl, it is chosen here for its wide industrial use. The Wall-Adapting Local Eddy-viscosity (WALE) model is chosen for the LES simulations with a filter width related to the local grid cell size, i.e. the cube root of cell volume in the present case. A second order discretization scheme is used both in space and time. In particular, the time discretization scheme used for the LES is second-order implicit backward Euler. The averaging of the flow quantities is started after 20 flow-through times (FT) and carried out for 40 FT, sampling each time step of the simulation. A plateau in the average static pressure is reached within the averaging time window and the simulation is stopped at the end of the 40 FT. The Courant-Friederichs-Levy (CFL) number is kept below unity to satisfy the stability requirements by using an adaptive time step. The time step, Δt, changes at each simulation iteration according to Eq. 1, in order to keep a maximum CFL number in the domain that does not exceed the user imposed value:

$$\Delta t = min\left(\frac{CFL}{\frac{1}{2V}\sum_{faces}|\phi_i|}\right), \tag{1}$$

where V is the cell volume, ϕ is the face volumetric flux and the summation is carried out over all cell faces. The factor $1/2$ assures the calculation of the average velocities. The computations require approximately 3 days on 40 cores for the LES simulations and one hour on 16 cores for the RANS ones. In particular, the Thinking cluster of the Vlaams Supercomputer Centrum [47] and an Intel Xeon workstation are used for the LES and RANS simulations, respectively. For the present test case, LES is thus about 2 orders of magnitude more expensive than RANS.

The obtained flow field characteristics are compared to the experimental measurements performed by Coletti et al. [39]. In particular, the normalized mean velocity field, $\overrightarrow{U}^\star$ (Eq. 2), and the normalized mean static pressure drop, $\Delta p^\star$ (Eq. 3), are compared to PIV visualizations and to static pressure measurements respectively,

$$\overrightarrow{U}^\star = \overrightarrow{U}\Big/U_0 \tag{2}$$

$$\Delta p^\star = \frac{p_{s,up} - p_{s,down}}{\frac{1}{2}\rho U_0^2} \tag{3}$$

where $p_{s,up}$ and $p_{s,down}$ are respectively the mean static pressure at the upstream and downstream measurement section, i.e. at a distance of $5D_h$ and $11D_h$ from the tip of the bend.

A comparison of the velocity field obtained in the middle plane, $z/D_h = 0.5$, with the different techniques is shown in Fig. 2. The PIV measurement, Fig. 2a, shows an acceleration of the flow around the inner-wall approaching the bend where the maximum velocity is reached, while a deceleration follows on the outer-wall. Along the internal bend a separation occurs and a recirculation region is formed as a result of the adverse pressure gradient caused by the bend curvature. The flow reattaches before the end of the bend. The RANS approach fails in the characterization of the separation region, which is largely underestimated (Fig. 2b). On the other hand, the LES simulation, Fig. 2c, confirms the experimental observations: both the velocity field and its streamline features are in agreement with the experimental ones. A slight overestimation of velocity magnitude is present on the inner-wall

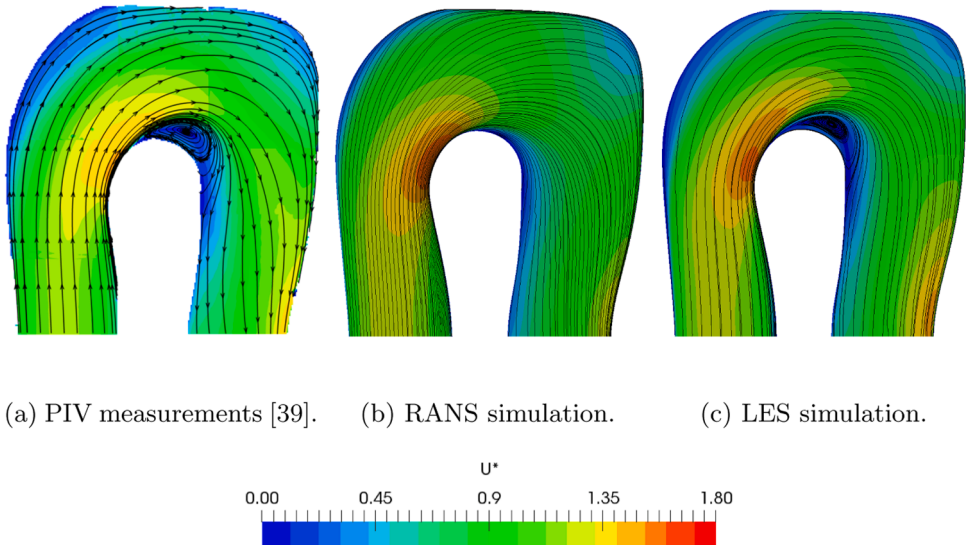

(a) PIV measurements [39]. (b) RANS simulation. (c) LES simulation.

Fig. 2. Normalized velocity field and its planar streamlines in the optimized U-bend ([38]) at $z/D_h = 0.5$.

before and around the recirculation region. The same behaviour is highlighted on the outer-wall at the end of the bend. Similar conclusions can be drawn for the comparison of the initial geometry [40].

The reference study considers the total pressure drop as objective function, therefore a reliable prediction is of paramount importance to drive the optimization to an improvement of the design. The comparison regards however the static pressure drop, as indicated in Eq. 3. Indeed, no variation between the static and the total pressure drop is expected at the planes considered, since the dynamic component of the total pressure is expected to be the same [38]. The $\Delta p^\star$ obtained with the different techniques is compared in Table 1, both for the initial and optimized bend of Verstraete et al. [38]. The absolute static pressure values obtained with RANS are largely overestimated for both geometries, while for LES they approach the values within the uncertainty interval of the experiments. Despite the inaccuracy of RANS to predict the absolute static pressure values, the relative improvement in the design by RANS (32.5%) is close to the one measured experimentally ($\sim$ 36.5%).

The pressure drop comparison highlights that the RANS approach fails in evaluating the absolute quantities but gives a reliable indication of the variation. This is further confirmed through the PIV data, that confirm that the precise flow field is not well captured by RANS, although the modifications suggested by the RANS-based optimization have guided the design to an improved flow field, reaching a gain close to the one measured experimentally. As a consequence, a first optimization with RANS is meaningful since an improved design can be obtained at a low computational cost. However, PIV data and LES have shown that a potential for further design improvements is present and could be achieved by removing the recirculation bubble. As a consequence, further improvements can only be obtained by a LES approach in the optimization phase, however this entails a significant larger computational cost.

Table 1
Normalized static pressure drop comparison.

$\Delta p^\star$	Experiment	RANS	LES
Standard	1.03 ± 0.03	1.26	1.08
Optimized	0.65 ± 0.02	0.85	0.72
Improvement [%]	36.5 ± 3	32.5	33.3

3. Towards LES-based optimization

The aim of the present work is to apply a LES-based optimization starting from the already optimized geometry of Verstraete et al. [38]. As the separation bubble has already been significantly reduced, only small changes are expected and therefore local gradient based optimization methods are more favourable. Despite the small design variations expected, many degrees of freedom need to be given to the shape to allow local adaptation for avoiding separation, which additionally favours gradient based methods.

As pointed out in the introduction, the direct application of the adjoint method to LES delivers unreliable gradients, therefore an another approach to include LES in the optimization loop is presented here. A general overview of the method is shown in Fig. 3. Initially, a LES simulation is performed on the initial geometry in order to have an accurate prediction of the flow field characteristics. The time averaged flow field from the LES is subsequently used to adapt a RANS model, such that the result of the RANS simulation approaches the LES time averaged flow field. This is achieved by adapting the turbulent viscosity,

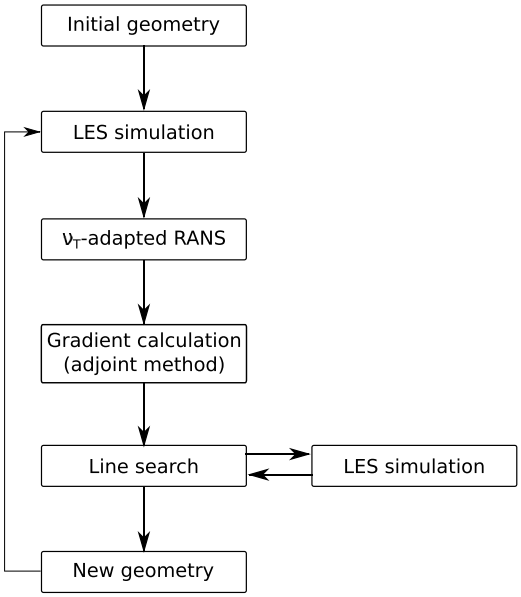

Fig. 3. LES-based optimization loop.

ν_t, in every cell of the domain. A detailed explanation of the procedure is expounded in Section 3.1. An adjoint approach is then used to compute the gradient with a frozen turbulence approach, hence considering ν_t invariant under shape modifications. This assumption, whose application can be found in many different works [20,48,49], allows to decouple the LES from the gradient evaluation procedure. Hence, only a differentiation of the steady state RANS model is required, which can be recuperated from a standard RANS based adjoint approach [2]. The adjoint solution then allows to compute the surface sensitivities, which indicate, under a linearised assumption, how the U-bend walls need to change for a reduced pressure loss. A line search is employed in the indicated search direction to determine the magnitude of the variation to apply. For each iteration of the line search a LES computation is performed. Details of the optimizer and of the line search approach are explained in Section 3.2. After evaluating the best step size for the movement, i.e. the magnitude of the geometry variation, the new geometry is obtained, which represents the starting point for the subsequent loop. The algorithm is terminated if after subsequent loops no significant further improvement is obtained.

The optimization loop proposed in Fig. 3 is a combination of two optimization strategies: an internal optimization loop which aims to improve the prediction of the RANS evaluation and an adjoint shape optimization. The ν_t-adaptation is repeated at each iteration of the optimization loop to ensure the proper evaluation of the turbulent viscosity, giving the correct flow field inside the design.

3.1. Turbulent viscosity adapted RANS

The LES is emulated by a computationally cheaper RANS simulation through specifying an inverse problem, in which the target is to retrieve as close as possible the average velocity obtained by LES ($\overline{U}_i$). A suitable objective function for the RANS velocity field (U_i) can be therefore defined as:

$$J = \int_\Omega \left(U_i - \overline{U}_i \right)^2 d\Omega \tag{4}$$

where Ω represents the computational volume.

A RANS solution closer to the LES one can be obtained by controlling the turbulent viscosity, ν_t, independently over the whole flow field. This allows to define an optimization problem in the control variable ν_t:

$$min \quad J(U, \nu_t) \tag{5}$$

subject to the RANS equations:

$$R^p(U, p, \nu_t) = -\frac{\partial U_j}{\partial x_j} = 0 \tag{6}$$

$$R_i^U(U, p, \nu_t) = U_j \frac{\partial U_i}{\partial x_j} - \frac{\partial}{\partial x_j}\left[\nu_{eff} \left(\frac{\partial U_i}{\partial x_j} + \frac{\partial U_j}{\partial x_i} \right) \right] + \frac{\partial p}{\partial x_i} = 0 \tag{7}$$

where ν_{eff} is the effective viscosity, given by the sum of the laminar and turbulent contribution $\nu_{eff} = \nu + \nu_t$. The RANS equations are specified as constraints and enforce that the mean velocity solution (U_i) satisfies them for the specified ν_t field. The approach still makes use of the Boussinesq approach, which assumes the isotropic behaviour of turbulence. This is a limitation of the methodology, as in general the flow field expected from the LES computation can yield large zones of non-isotropic turbulence. Further improvements to the methodology are thus possible by deviating from the Boussinesq approach. In the present work, however, as a proof of concept, the Boussinesq approach is kept which as a result will limit the potential reduction of the objective function defined in Eq. 4.

To solve the optimization problem defined by Eq. 5–7, a gradient based method is applied for which the adjoint method is used for the calculation of the gradient. The flow chart of the ν_t-adaptation of the RANS model is shown in Fig. 4. Turbulence models are not used in the solution of the RANS equations: they are indeed not necessary as the turbulent viscosity is adapted according to the gradient of the objective function to minimize. The solution of the adjoint equations follows the RANS evaluation. When both systems of equations are solved, it is possible to evaluate the turbulent viscosity sensitivity which indicates how to modify the turbulent viscosity in each cell of the domain in order to minimize the objective function. In the present work, a steepest descent algorithm is then used to update the turbulent viscosity [50]. To speed-up the convergence of the whole loop, starting from an initial fully converged RANS solution, each individual solution of the RANS and adjoint equations is not fully converged and a one-shot approach [51] is used.

A classical approach to solve the optimization problem defined by Eq. 5–7 consists in the use of Lagrangian multipliers. In particular, for a general objective function J, the augemtented objective function L is introduced as:

$$L = J + \int_\Omega q R^p \, d\Omega + \int_\Omega U_{ai} R_i^U \, d\Omega \tag{8}$$

where q and U_{ai} are Lagrancian multipliers, termed respectively the adjoint pressure and adjoint velocity. The variation of the objective function with respect to an arbitrary control variable b_n, which identifies the improvement direction, can be computed as:

$$\frac{\delta L}{\delta b_n} = \frac{\delta J}{\delta b_n} + \frac{\delta}{\delta b_n}\int_\Omega q R^p \, d\Omega + \frac{\delta}{\delta b_n}\int_\Omega U_{ai} R_i^U \, d\Omega \tag{9}$$

Considering the turbulent viscosity as control variable ($b_n = \nu_t$), applying the Leibniz theorem and considering the equality given by Eq. 6 and Eq. 7, this results in:

$$\frac{\delta L}{\delta \nu_t} = \frac{\delta J}{\delta \nu_t} + \int_\Omega q \frac{\partial R^p}{\partial \nu_t} \, d\Omega + \int_\Omega U_{ai} \frac{\partial R_i^U}{\partial \nu_t} \, d\Omega \tag{10}$$

The three terms on the r.h.s of Eq. 10 can be further developed. In particular, considering the chain rule, the first term becomes:

$$\frac{\delta J}{\delta \nu_t} = \int_\Omega \frac{\partial J_\Omega}{\partial U_i}\frac{\partial U_i}{\partial \nu_t} \, d\Omega + \int_\Gamma \frac{\partial J_\Gamma}{\partial U_i}\frac{\partial U_i}{\partial \nu_t} \, d\Gamma + \int_\Omega \frac{\partial J_\Omega}{\partial p}\frac{\partial p}{\partial \nu_t} \, d\Omega + \int_\Gamma \frac{\partial J_\Gamma}{\partial p}\frac{\partial p}{\partial \nu_t} \, d\Gamma \tag{11}$$

where Γ represents the boundary of the computational domain, J_Ω and J_Γ represent the objective function contributions in the volume and on the boundaries respectively. By applying permutation and the Gauss divergence theorem, the second term of the r.h.s. of Eq. 10 becomes:

$$\int_\Omega q \frac{\partial R^p}{\partial \nu_t} \, d\Omega = -\int_\Omega q \frac{\partial}{\partial \nu_t}\left(\frac{\partial U_j}{\partial x_j} \right) d\Omega = -\int_\Gamma q \frac{\partial U_j}{\partial \nu_t} n_j \, d\Gamma + \int_\Omega \frac{\partial q}{\partial x_j}\frac{\partial U_j}{\partial \nu_t} \, d\Omega \tag{12}$$

The third therm of the r.h.s. of Eq. 10 can be written as:

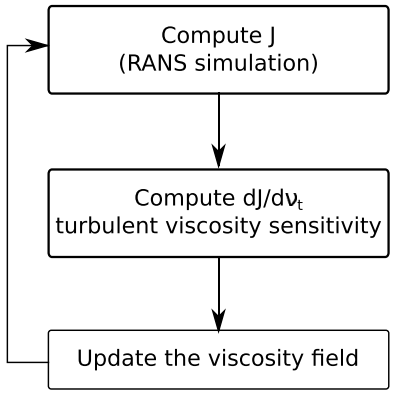

Fig. 4. ν_t-adaptation loop.

$$\int_\Omega U_{ai}\frac{\partial R_i^U}{\partial \nu_t}\,d\Omega = \int_\Omega U_{ai}\frac{\partial}{\partial \nu_t}\left(U_j\frac{\partial U_i}{\partial x_j}\right)d\Omega - \int_\Omega U_{ai}\frac{\partial}{\partial \nu_t}\left\{\frac{\partial}{\partial x_j}\left[\nu_{eff}\left(\frac{\partial U_i}{\partial x_j}+\frac{\partial U_j}{\partial x_i}\right)\right]\right\}d\Omega + \int_\Omega U_{ai}\frac{\partial}{\partial \nu_t}\left(\frac{\partial p}{\partial x_i}\right)d\Omega. \tag{13}$$

The three terms on the r.h.s. in the equality of Eq. 13 ($b1$, $b2$ and $b3$ respectively) can be further developed applying permutation and the Gauss divergence theorem, such that:

$$b1 = \int_\Omega U_{ai}\frac{\partial U_i}{\partial x_j}\frac{\partial U_j}{\partial \nu_t}\,d\Omega + \int_\Gamma U_{ai}U_j n_j\frac{\partial U_i}{\partial \nu_t}\,d\Gamma - \int_\Omega \frac{\partial\left(U_{ai}U_j\right)}{\partial x_j}\frac{\partial U_i}{\partial \nu_t}\,d\Omega \tag{14}$$

$$\begin{aligned} b2 &= -\int_\Omega U_{ai}\frac{\partial}{\partial x_j}\left(\frac{\partial U_i}{\partial x_j}+\frac{\partial U_j}{\partial x_i}\right)d\Omega - \int_\Omega U_{ai}\frac{\partial}{\partial x_j}\left[\nu_{eff}\frac{\partial}{\partial \nu_t}\left(\frac{\partial U_i}{\partial x_j}+\frac{\partial U_j}{\partial x_i}\right)\right]d\Omega \\ &= -\int_\Omega U_{ai}\frac{\partial}{\partial x_j}\left(\frac{\partial U_i}{\partial x_j}+\frac{\partial U_j}{\partial x_i}\right)d\Omega - \int_\Gamma U_{ai}n_j\nu_{eff}\frac{\partial}{\partial \nu_t}\left(\frac{\partial U_i}{\partial x_j}+\frac{\partial U_j}{\partial x_i}\right)d\Gamma \\ &+\int_\Gamma \nu_{eff}\left(\frac{\partial U_{ai}}{\partial x_j}+\frac{\partial U_{aj}}{\partial x_i}\right)n_j\frac{\partial U_i}{\partial \nu_t}\,d\Gamma - \int_\Omega\frac{\partial}{\partial x_j}\left[\nu_{eff}\left(\frac{\partial U_{ai}}{\partial x_j}+\frac{\partial U_{aj}}{\partial x_i}\right)\right]\frac{\partial U_i}{\partial \nu_t}\,d\Omega \end{aligned} \tag{15}$$

$$b3 = \int_\Gamma U_{ai}n_i\frac{\partial p}{\partial \nu_t}\,d\Gamma - \int_\Omega \frac{\partial U_{ai}}{\partial x_i}\frac{\partial p}{\partial \nu_t}\,d\Omega \tag{16}$$

Substituting Eq. 11, Eq. 12 and Eq. 13 (considering the equality in Eq. 14, Eq. 15 and Eq. 16) into Eq. 10, the variation of the augmented objective function with respect to the control variable, i.e. the turbulent viscosity, is obtained:

$$\begin{aligned} \frac{\delta L}{\delta \nu_t} &= \int_\Omega\frac{\partial J_\Omega}{\partial U_i}\frac{\partial U_i}{\partial \nu_t}\,d\Omega + \int_\Omega\frac{\partial J_\Omega}{\partial p}\frac{\partial p}{\partial \nu_t}\,d\Omega + \int_\Omega\frac{\partial q}{\partial x_j}\frac{\partial U_j}{\partial \nu_t}\,d\Omega + \int_\Omega U_{ai}\frac{\partial U_i}{\partial x_j}\frac{\partial U_j}{\partial \nu_t}\,d\Omega \\ &-\int_\Omega\frac{\partial\left(U_{ai}U_j\right)}{\partial x_j}\frac{\partial U_i}{\partial \nu_t}\,d\Omega - \int_\Omega U_{ai}\frac{\partial}{\partial x_j}\left(\frac{\partial U_i}{\partial x_j}+\frac{\partial U_j}{\partial x_i}\right)d\Omega - \int_\Omega\frac{\partial U_{ai}}{\partial x_i}\frac{\partial p}{\partial \nu_t}\,d\Omega \\ &-\int_\Omega\frac{\partial}{\partial x_j}\left[\nu_{eff}\left(\frac{\partial U_{ai}}{\partial x_j}+\frac{\partial U_{aj}}{\partial x_i}\right)\right]\frac{\partial U_i}{\partial \nu_t}\,d\Omega \\ &+\int_\Gamma\frac{\partial J_\Gamma}{\partial U_i}\frac{\partial U_i}{\partial \nu_t}\,d\Gamma + \int_\Gamma\frac{\partial J_\Gamma}{\partial p}\frac{\partial p}{\partial \nu_t}\,d\Gamma - \int_\Gamma q\frac{\partial U_j}{\partial \nu_t}n_j\,d\Gamma + \int_\Gamma U_{ai}U_jn_j\frac{\partial U_i}{\partial \nu_t}\,d\Gamma \\ &-\int_\Gamma U_{ai}n_j\nu_{eff}\frac{\partial}{\partial \nu_t}\left(\frac{\partial U_i}{\partial x_j}+\frac{\partial U_j}{\partial x_i}\right)d\Gamma + \int_\Gamma\nu_{eff}\left(\frac{\partial U_{ai}}{\partial x_j}+\frac{\partial U_{aj}}{\partial x_i}\right)n_j\frac{\partial U_i}{\partial \nu_t}\,d\Gamma \\ &+\int_\Gamma U_{ai}n_i\frac{\partial p}{\partial \nu_t}\,d\Gamma. \end{aligned} \tag{17}$$

So far the Lagrange multipliers q and U_{ai} are still to be chosen freely. As the evaluation of the derivatives of the flow variables w.r.t. the control variable are expensive to evaluate, it is common to group the volume integrals that involve those derivatives and set them to zero, thus establishing a system of equations involving the Lagrange multipliers:

$$-\frac{\partial U_{ai}}{\partial x_i}+\frac{\partial J_\Omega}{\partial p} = 0 \tag{18}$$

$$U_{ai}\frac{\partial U_i}{\partial x_j} - \frac{\partial\left(U_{ai}U_j\right)}{\partial x_j} - \frac{\partial}{\partial x_j}\left[\nu_{eff}\left(\frac{\partial U_{ai}}{\partial x_j}+\frac{\partial U_{aj}}{\partial x_i}\right)\right] + \frac{\partial q}{\partial x_j}+\frac{\partial J_\Omega}{\partial U_i} = 0 \tag{19}$$

The equations above, Eq. 18 and Eq. 19, are called the adjoint continuity and the adjoint momentum equation, respectively.

The boundary conditions necessary to solve the adjoint equations can be obtained from the surface integrals in Eq. 17. In particular, the derivation corresponding to some typical boundary condition for the flow field is as follows:

- **Inlet and walls**. Usually a Dirichlet boundary condition is chosen for the velocity, as a consequence all the terms involving the surface integral of the derivative of the flow velocity w.r.t. the control variable vanish since $\frac{\partial U_i}{\partial \nu_t} = 0$. On the other hand, the boundary condition for the pressure is of Neumann type, thus $\frac{\partial p}{\partial \nu_t} \neq 0$. Therefore, the boundary condition to set for the adjoint velocity is obtained by setting the terms involving those derivatives to zero. The boundary condition for the adjoint pressure is set in accordance with the pressure boundary condition:

$$\begin{aligned} U_{ai}n_i + \frac{\partial J_\Gamma}{\partial p} &= 0, \\ U_{ai}n_j &= 0, \\ \frac{\partial q}{\partial x_i} &= 0. \end{aligned} \tag{20}$$

- **Outlet**. A Dirichlet boundary condition is commonly used for the pressure, i.e. $\frac{\partial p}{\partial \nu_t} = 0$, thus the according terms vanish. Moreover, assuming an uniform velocity profile as the outlet section is far enough from the bend, the integral containing $\frac{\partial U_i}{\partial x_j}+\frac{\partial U_j}{\partial x_i}$ is zero. A Neumann boundary condition is typically applied to the velocity, as a result $\frac{\partial U_i}{\partial \nu_t} \neq 0$. As a consequence, the surface integrals containing these derivatives give the adjoint boundary conditions for the adjoint pressure and for the tangential adjoint velocity by setting the multiplying terms to zero. The adjoint velocity normal to the boundary is extracted from the internal domain.

$$-qn_j + U_{ai}U_jn_j + \nu_{eff}\left(\frac{\partial U_{ai}}{\partial x_j}+\frac{\partial U_{aj}}{\partial x_i}\right)n_j + \frac{\partial J_\Gamma}{\partial U_i} = 0 \tag{21}$$

The adjoint equations, Eq. 18 and Eq. 19, and their boundary conditions, Eq. 20 and Eq. 21, depend on the objective function chosen. In the present work, this is the difference between the velocity field obtained with a RANS evaluation, U_i, and the mean velocity obtained with a LES one, $\overline{U}_i$. Because the objective function, defined in Eq. 4, is a volumetric objective function, its derivative on the boundaries is zero. The terms in Eq. 22 complete the adjoint equations and the adjoint boundary conditions.

$$\frac{\partial J_\Omega}{\partial U_i} = 2\left(U_i-\overline{U}_i\right) \quad ; \quad \frac{\partial J_\Omega}{\partial p} = 0 \quad ; \quad \frac{\partial J_\Gamma}{\partial U_i} = 0 \quad ; \quad \frac{\partial J_\Gamma}{\partial p} = 0 \tag{22}$$

The solution of the adjoint equations, Eq. 18 and Eq. 19, with their boundary conditions, Eq. 20 and Eq. 21, allows the evaluation of the adjoint variables, U_a and q, and reduces equation Eq. 17 to one term only:

$$\frac{\delta L}{\delta \nu_t} = \frac{\delta J}{\delta \nu_t} = -U_{ai}\frac{\partial}{\partial x_j}\left(\frac{\partial U_i}{\partial x_j}+\frac{\partial U_j}{\partial x_i}\right) \tag{23}$$

because the gradient of L is identical to the gradient of J when Eq. 6 and Eq. 7 are satisfied. The above expression represents the sensitivity of the objective function J with respect to the control variable ν_t, and thus identifies how to adjust the control value to reduce the objective function.

A steepest descent algorithm is used to minimize J. To prevent non-physical values, the steepest descent algorithm is modified to ensure that the value of ν_t is clipped between $\nu_t^{\min}$ and $\nu_t^{\max}$,

$$\nu_t^{New} = \min\left[\max\left(\nu_t^T + \lambda\frac{\delta J}{\delta \nu_t}, \nu_t^{min}\right), \nu_t^{max}\right] \tag{24}$$

where λ defines the step size of the control variable modifications.

Negative turbulent viscosity values are prevented by imposing $\nu_t^{\min} = 0$, while enforcing a maximum limit ($\nu_t^{\max}$) avoids a divergent solution. A relaxation factor γ is used to help the solution convergence,

$$\nu_t^{T+1} = (1-\gamma)\nu_t^T + \gamma\nu_t^{New} \tag{25}$$

where the superscripts T and $T+1$ refer to two consecutive iterations.

The described approach is general and can be applied to all flows suitable for an adjoint optimization strategy. The test case presented in this paper has a starting flow field which is similar to the target one, facilitating the optimizer in reaching the desired flow field characteristics (i.e. the creation of the recirculation bubble). However, from a theoretical point of the view, this approach would work also if the RANS solution is very far from the LES one. When the RANS and LES solutions differ considerably from each other, an optimized solution closer to the LES than the RANS one would be still obtained although the discrepancies between the optimized and LES solution could be still significant.

3.2. Node-based shape routine and line search approach

The resulting flow field obtained from the ν_t-adapted RANS is then used for the evaluation of the adjoint field in the context of a shape optimization problem in which the objective is the minimization of the pressure losses. Thus, the considered objective function J is now represented by:

$$J = p_T^{in} - p_T^{out} = \int_{\Gamma_{in}} p + \frac{1}{2}\rho U^2 \, d\Gamma - \int_{\Gamma_{out}} p + \frac{1}{2}\rho U^2 \, d\Gamma, \tag{26}$$

where p_T represents the total pressure and *in* and *out* refer to the inlet and outlet boundary of the domain respectively.

In particular, the node-based adjoint optimization routine by Alessi et al. [52] is used in this work. The adjoint equations for shape optimization and pressure loss reduction are solved using a frozen turbulent approach and, in particular, using the optimal turbulent viscosity field obtained as a result of the inverse problem. The control variables chosen at the present step of the LES-based optimization are represented by the normal displacement of each surface node, resulting in a very rich design space. As a consequence, the surface sensitivity map obtained from the solution of the adjoint and RANS equations expresses how much the objective function would change for a unit movement in the direction of the surface normal. Before converting the gradient information into a design variation, a Gaussian filter is applied to damp short wavelength oscillations [53]. The attainment of a smooth sensitivity is a crucial point to obtain a valid geometry deformation, and thus an admissible design. Therefore, the use of a filter is indispensable. The filtered surface sensitivity is linked with a steepest descent algorithm to modify every node of the U-bend wall and obtain the newly optimized design, as follows:

$$\mathbf{x^{i+1}} = \mathbf{x^i} + \beta\bar{S}\mathbf{n}, \tag{27}$$

where $\mathbf{x^i}$ and $\mathbf{x^{i+1}}$ represent the position vector of each node before and after the boundary movement respectively. Each node is displaced in the direction normal to the surface, $\mathbf{n}$, with a magnitude depending on the smoothed surface sensitivity, $\bar{S}$. The parameter β represents the step size of the algorithm. The optimizer guarantees a smooth design and the compliance of constraints, if present. Similar to the optimization in reference [38], no movement is allowed in the z direction and a bounding box surrounding the bend defines the geometrical constraints. In-plane modifications of the bend are possible in order to take full advantage of the potential of a node-based optimization, different from the reference case where only 26 degrees of freedom are given to the parametrized model of the U-bend. In addition, in agreement with the work of Verstraete et al. [38], the inlet and outlet leg of the bend remain fixed for a length of $8D_h$ and only the remaining regions close to the bend take part in the optimization process.

The reason for the choice of the steepest descent algorithm lies in its ease of implementation. However, the choice of a suitable step size for the optimization represents a drawback, which could lead to a long convergence time and consequently to waste of computational resources. In order to mitigate the aforementioned disadvantage, a line search strategy is added to the steepest descent algorithm to speed-up the optimization process. The idea behind the line search is to vary the step size for a given iteration, in order to find the one that minimizes the objective function in the descent direction given by the sensitivity. In particular, starting from an initial guess, β^*, the step magnitude is increased and decreased by a factor of 1.5. The performance of the three different geometries is evaluated in search for the minimum of the objective function. If a minimum is not identified, the step size is changed in the direction of performance increase until the identification of the geometry with the best performance, stating the end of the line search for the iteration considered. The corresponding step magnitude is used as initial guess for the line search of the next optimization iteration. A LES simulation is carried out at each step of the line search in order to have an accurate prediction of the objective function.

The last step of the optimization process is represented by a link between the boundary movement and the mesh deformation. In the present work is used a mesh morpher based on the Laplace equation in which the prescribed boundary movement represents the boundary condition for the internal cell motion. The diffusivity in the Laplace equation is equal to the inverse square distance from the nearest boundary. A distance-based diffusivity improves the mesh quality near the boundaries: it redistributes the movement inside the domain allowing bigger deformations on the center of the domain where bigger cells are present. Details on the used optimizer, smoothing operations, the attainment of constraints and mesh deformation strategy can be found in Alessi et al. [52].

4. Optimization results of the LES-based optimization

The previously outlined algorithms define an optimization strategy within a LES context. The methodology is applied to the U-bend test case optimized in Verstraete et al. [38] and aims to reach further improvements by a more accurate evaluation of the flow field.

4.1. Results of the ν_t-adapted RANS

The first step of the proposed approach aims to fit the LES time

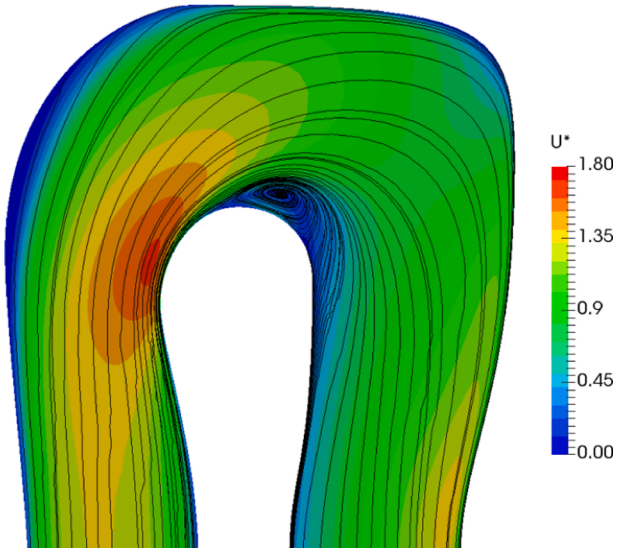

Fig. 5. Normalized velocity field and its planar streamlines in the ν_t-adapted RANS solution at $z/D_h = 0.5$.

averaged flow field with a RANS calculation through the solution of an inverse problem. The output of the ν_t-adapted RANS solution is shown in Fig. 5. It concerns the first loop of the optimization algorithm, therefore it refers to the initial geometry taken into account and analyzed in Fig. 2. In particular, Fig. 5 shows the velocity field at the middle plane $z = 0.5D_h$. The planar streamlines highlight the formation of a recirculation bubble in the internal bend region, recovering the correct fluid structures inside the bend shown in the PIV visualization (Fig. 2a). A comparison between Fig. 2c and Fig. 5 shows a very good agreement between the solution obtained with the LES and ν_t-adapted RANS. Approaching the internal bend, a slight overestimation of velocity magnitude is present in the ν_t-adapted RANS solution in comparison with the LES one. On the other hand, slightly slower velocity regions are obtained in the outer side of the bend. The cell-based variation of the turbulent viscosity allows therefore to obtain a RANS solution very similar to the LES one.

The turbulent viscosity field at the middle plane resulting from the solution of the inverse problem and its comparison with the field obtained from a standard RANS simulation is shown in Fig. 6. In particular, the colorbar range of the two fields is saturated to a value of $\nu_t = 3{\cdot}10^{-3}$ to highlight the differences. The ν_t-adapted field is very similar to the standard field with differences in a few regions. An increase of turbulent viscosity is present close to the inner-wall at the bend entrance (label A in Fig. 6b), which is the main region to be modified in order to recreate the recirculation region. The viscosity increment represents an obstacle to the flow promoting the flow separation. Due to the obstruction, the region of maximum velocity shifts from occupying a large region along the wall (Fig. 2b) to a slightly detached location (Fig. 5). Differences can be also noted in the region of the now properly represented flow recirculation. A comparison between the RANS and LES solution, Fig. 2b and Fig. 2c respectively, shows a difference in the velocity field at the outer-wall region of the inlet leg. The bigger zone with low velocity in the LES simulation is now well represented due to an increase of turbulence viscosity in the ν_t-adapted RANS simulation. A local adaptation of the viscosity field is therefore capable of adjusting the regions of main differences between the RANS and LES velocity field.

The ν_t-adaptation convergence history is shown in Fig. 7, where the evolution of the objective function in Eq. 4 with iteration number is plotted. The optimization history shows a fast reduction of the objective function, which reaches its minimum value in approximately 1000 iterations. However, the ν_t distribution found is not associated to a convergent flow field. The residuals of the flow field and adjoint equations decrease indeed for 5000 iterations. After that, the residuals gradually stabilize and no variation on the shape of the newly created recirculation bubble is observed in the last two thousand iterations. A plateau identifies the end of the optimization process, which establishes that a reduction of 41.6% in J is achieved in 8000 iterations. The solution of the ν_t-adaptation problem requires 3 hours using 16 cores.

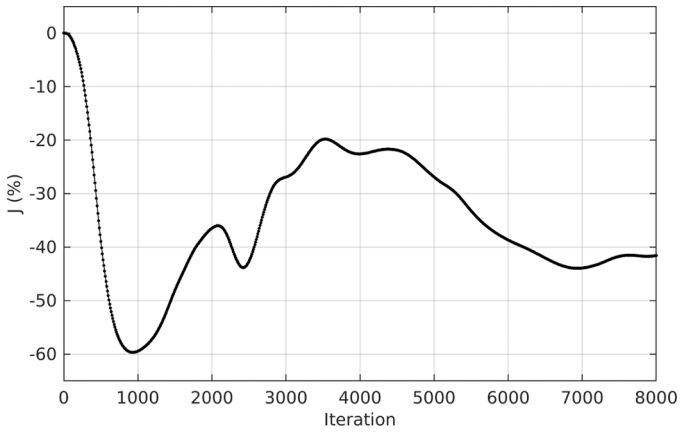

Fig. 7. Convergence history of the objective function in the ν_t-adaptation process.

4.2. Results of the LES-based optimization

The ν_t-adaptation methodology provides a more correct flow field and can be used in combination with the adjoint shape optimization routine, such that the LES is not involved in the gradient evaluation procedure. The objective is now the reduction of the total pressure drop, using the optimization loop in Fig. 3. As no variation between the static and the total pressure drop is expected at the planes considered, the loop is solved until no further gains in static pressure drop are obtained. The latter can be monitored by the optimization history curve shown in Fig. 8. Each iteration corresponds to one whole loop of the algorithm, which includes a line search. A large improvement in performance is already obtained by the first iteration, with an additional gain in terms of static pressure drop of $\Delta p = -2.97\%$ on a previously optimized design. The successive iterations essentially confirm the first one, as the following designs display comparable performances. As the starting design comes from a previous optimization [38], only very small modifications would be expected after the first iteration of the optimization loop in which a line search approach is used. The strategies employed to ensure a smooth design further reduce the modifications at the second iteration of the optimization loop and at the successive ones, resulting in a similar geometry to the one obtained at the first iteration, with a similar performance. The computational time is approximately 4 days per optimization loop iteration on 40 cores.

The line search corresponding to the first major iteration is shown in Fig. 9. Starting from an initial guess, $\beta^* = 0.066D_h$, a descent direction in the value of the static pressure drop is present with an increase of the step size until a minimum is obtained at $\beta = 2\beta^* = 0.132D_h$. This step

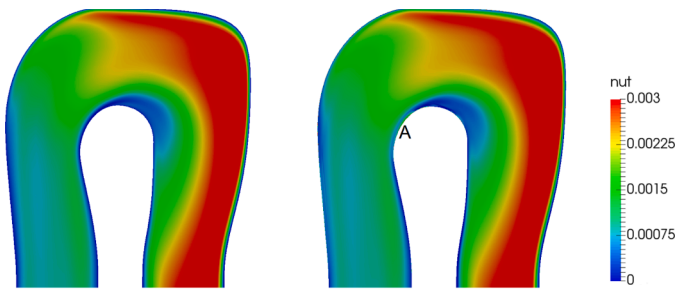

(a) RANS solution. (b) ν_t-adapted RANS solution.

Fig. 6. Turbulent viscosity field at $z/D_h = 0.5$ (initial geometry).

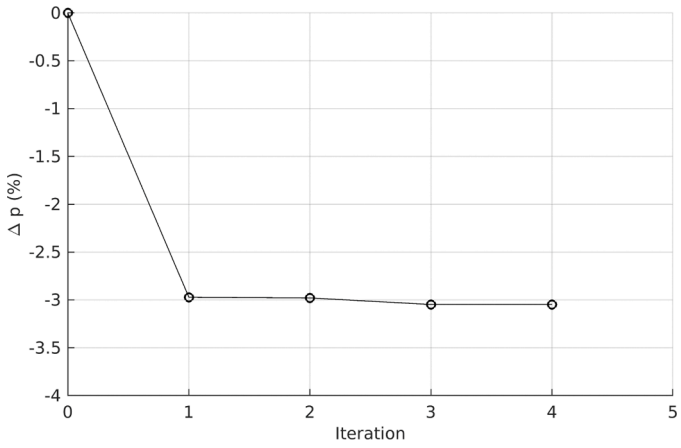

Fig. 8. LES-based optimization history.

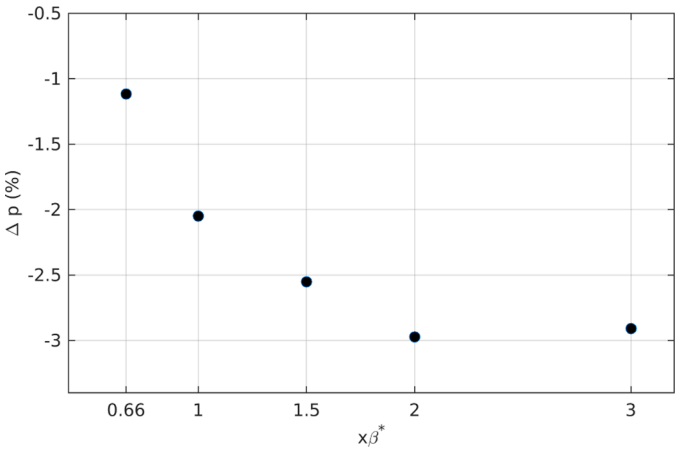

Fig. 9. Line search result of the first major iteration.

size identifies the design corresponding to the best performance achievable in the searched direction and is used as initial guess for the next optimization loop iteration. Its geometry is adopted as starting point for the subsequent major iteration.

The obtained optimized design is shown in Fig. 10. In particular, a comparison between the initial and the optimized U-bend, respectively in black and in red, is shown at two different planes: at $z/D_h = 0.5$ in Fig. 10a and at the yz plane in Fig. 10b. The comparison highlights how small modifications are sufficient to obtain a remarkable performance improvement. The two designs are indeed very close to each other and only few modifications are applied to obtain the LES-based optimized design. This was however expected since the starting U-bend is the result of a previous RANS-based optimization study ([38]) and thus its geometry is already close to the optimal one. The small modifications applied are however sufficient to obtain an improved design, squeezing the last percentage of performance improvement. The variations affect almost exclusively the internal bend region, as shown in both planes illustrated. A small asymmetry in the shape with respect to the middle plane is highlighted in Fig. 10b. Indeed, the mean velocity field obtained from the LES simulation and consequently the one from the ν_t-adapted RANS approach shows small asymmetries that affect the surface sensitivity information and, as consequence, the geometry movement. This could be improved by imposing symmetry in the geometry deformation and averaging the surface sensitivities from the top and bottom symmetric sides, which is however not performed in the present work.

The normalized mean velocity field from the LES simulation with its planar streamlines at the middle plane in the newly optimized geometry is shown in Fig. 11. A comparison between the mean velocity field of the initial design, Fig. 2c, and the one obtained after the optimization process, Fig. 11, confirms that the modifications performed by the optimizer effectively decrease the total pressure drop in the design by reducing the recirculation bubble, which almost disappears. The modifications in the design concern the entry region of the internal bend, as shown in Fig. 10a, which now better guides the flow in the bend. As a consequence, a decrease of the maximum mean velocity is obtained around the inner bend in comparison with the initial geometry, resulting in a lower adverse pressure gradient and in the consequent reduction of the separation region size. This is confirmed by the comparison of the normalized static pressure field at $z/D_h = 0.5$ shown in Fig. 12. The region of adverse pressure gradient around the bend that is present in the initial geometry (Fig. 12a) is considerably reduced in the ν_t-adapted RANS optimized geometry (Fig. 12b), resulting in the reduction of the size of the separation region.

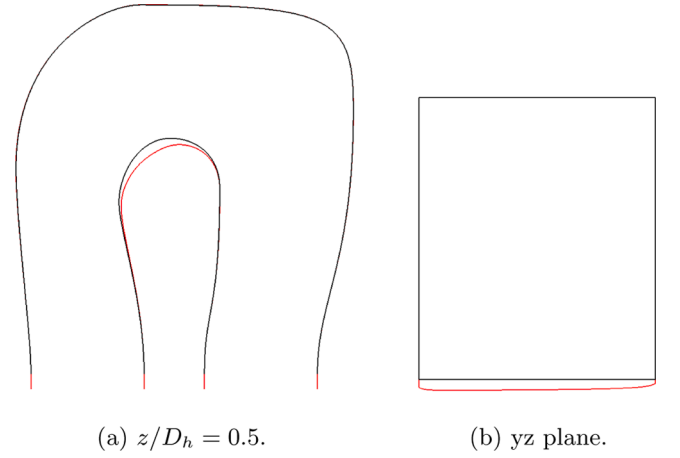

Fig. 10. Comparison between initial (black) and optimized U-bend (red). (For interpretation of the references to colour in this figure legend, the reader is referred to the web version of this article.)

5. Conclusions

The use of the RANS approach to evaluate the flow field characteristics in an optimization framework could lead to inaccurate results. A comparison between the mean velocity field obtained with RANS and LES and the experimental data available in literature shows that the RANS approach fails to correctly evaluate the flow features inside a U-bend geometry. A validation study in an optimized geometry highlights the presence of a recirculation region inside the bend both in the experiments and in the LES simulation, while it is not detected by a RANS evaluation. The separation region is responsible for additional pressure losses inside the system and its elimination would bring an improvement to the design, which could only be achieved by using a LES based approach.

The present work therefore proposes a new approach for the introduction of LES in an optimization framework, by using the adjoint method to keep the number of expensive LES computations to a minimum. As the direct application of the adjoint approach would lead to unreliable sensitivities, an additional step to detach the LES from the gradient computations is developed and introduced in the optimization loop. Starting from a RANS simulation, an adaptation process of the turbulent viscosity is carried out aiming to obtain a velocity field that

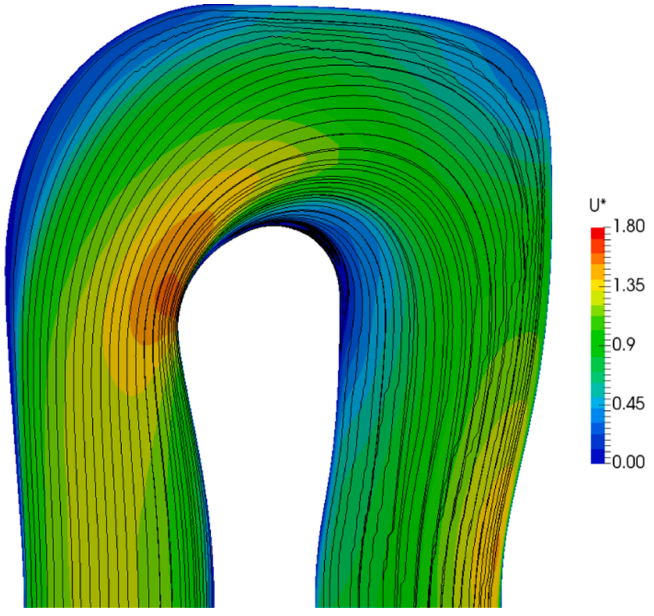

Fig. 11. Normalized mean velocity field and its planar streamlines for the LES-based optimized U-bend at $z/D_h = 0.5$.

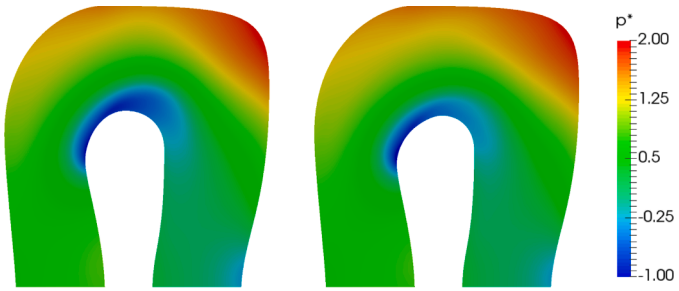

(a) Initial geometry. (b) ν_t-adapted RANS optimized geometry.

Fig. 12. Normalized mean static pressure at $z/D_h = 0.5$.

represents the mean velocity field coming from a LES solution. The results show that the proposed approach can overcome the limitations of the original RANS solution, as with an adaptation of the turbulent viscosity a mean velocity field very similar to the experimental one can be obtained. This solution is then used as the starting point for an adjoint shape optimization routine to further improve the design based on LES evaluations. The obtained design has an additional 3% reduction in total pressure drop compared to a previously optimized geometry. The optimizer aims to reduce the total pressure drop by reducing the recirculation region inside the bend, confirming that an accurate evaluation of the mean velocity field inside the bend is of fundamental importance. The computational cost of the proposed approach based on LES evaluations is considerably higher than the one based on RANS simulations, approximately 96 and 12 hours respectively. As a consequence, a first optimization with RANS should be carried out, since it allows to obtain an optimized design at a low computational cost. The design obtained can be then fine-tuned and further improved by considering the LES-based approach.

The proposed approach allows to integrate LES evaluations in an adjoint optimization routine, providing reliable gradient information. This results in optima that are more effective in real operating conditions, as the optimization uses accurate flow field predictions.

CRediT authorship contribution statement

G. Alessi: Conceptualization, Software, Validation, Formal analysis, Writing – original draft. **T. Verstraete:** Methodology, Validation, Resources, Writing – review & editing, Supervision. **L. Koloszar:** Software, Validation, Writing – review & editing, Supervision. **B. Blocken:** Validation, Writing – review & editing, Supervision. **J.P.A.J. van Beeck:** Validation, Writing – review & editing, Supervision.

Declaration of Competing Interest

None.

Acknowledgement

This work was supported by the Fonds Wetenschappelijk Onderzoek Vlaanderen - FWO (SB Fellowship 1S 581 16N).

References

[1] Thevenin D, Janiga G. Optimization and computational fluid dynamics. Springer-Verlag Berlin Heidelberg; 2008.
[2] Papoutsis-Kiachagias E, Giannakoglou K. Continuous adjoint methods for turbulent flows, applied to shape and topology optimization: industrial applications. Arch Comput Methods Eng 2016;23(2):225–99.
[3] Hirsch C, Tartinville B. Reynolds-averaged navier-stokes modelling for industrial applications and some challenging issues. Int J Comut Fluid Dyn 2009;23(4):295–303.
[4] Corson D, Jaiman R, Shakib F. Industrial application of RANS modelling: capabilities and needs. Int J Comut Fluid Dyn 2009;23(4):337–47.
[5] Blocken B. LES Over RANS in building simulation for outdoor and indoor applications: a foregone conclusion? Build Simul 2018;11(5):821–70.
[6] Marsden A, Wang M, Dennis J, Moin P. Trailing-edge noise reduction using derivative-free optimization and large-eddy simulation. J Fluid Mech 2007;572:13–36.
[7] Goit J, Meyers J. Optimal control of wind farm power extraction in large eddy simulations. AIAA SciTech 32nd ASME Wind Energy Symposium 2014:AIAA2014–0709.
[8] Collis S, Chang Y. Computer simulation of active control in complex turbulent flows. Model Simulat Eng 2000;I:851–6.
[9] Lions J. Optimal control of systems governed by partial differential equations. Springer Berlin Heidelberg; 1971.
[10] Pironneau O. On optimum design in fluid mechanics. J Fluid Mech 1974;64 part I:97–110.
[11] Jameson A. Aerodynamic design via control theory. J Sci Comput 1988;3(3):233–60.
[12] Brezillon J, Dwight R, Widhalm M. Aerodynamic optimization for cruise and high-lift configurations. MEGADESIGN and MegaOpt - German Initiatives for Aerodynamic Simulation and Optimization in Aircraft Design 2009:249–62.
[13] Jameson A, Pierce N, Martinelli L. Optimum aerodynamic design using the navier-stokes equations. Theor Comput Fluid Dyn 1998;10:213–37.
[14] Martins J, Alonso J, Reuther J. A coupled-adjoint sensitivity analysis method for high-fidelity aero-structural design. Opt Eng 2005;6:33–62.
[15] Elham A, Van tooren M. Coupled adjoint aerostructural wing optimization using quasi-three-dimensional aerodynamic analysis. Struct Multidiscip Optim 2016;54(4):889–906.
[16] Mueller L, Verstraete T. Adjoint-based multi-point and multi-objective optimization of a turbocharger radial turbine. Int J Turbomachin Propulsion Power 2019;4(2):10.
[17] Verstraete T, Muller L, Muller J. Adjoint-based design optimisation of an internal cooling channel u-bend for minimised pressure losses. Int J Turbomachin Propulsion Power 2017;2(2):10.
[18] Karpouzas G, Papoutsis-Kiachagias E, Schumacher T, de Villiers E, Giannakoglou K, C., Othmer. Adjoint optimization for vehicle external aerodynamics. Int J Automot Eng 2016;7:1–7.
[19] Othmer C. Adjoint methods for car aerodynamics. Math Ind 2014;4:6.
[20] Helgason E, Krajnovic S. Aerodynamic shape optimization of a pipe using the adjoint method. Proc ASME 2012 Int Mech Eng Congress Exposit 2012:IMECE2012.
[21] Stuck A, Rung T. Adjoint RANS with filtered shape derivatives for hydrodynamic optimisation. Comput Fluid 2011;47(1):22–32.
[22] Gkaragkounis K, Papoutsis-Kiachagias E, Giannakoglou K. The continuous adjoint method for shape optimization in conjugate heat transfer problems with turbulent incompressible flows. Appl Therm Eng 2018;140:351–62.
[23] Subramaniam V. Topology optimization of conjugated heat transfer devices: experimental and numerical investigation. IMT Lille Douai: Ph.D. dissertation; 2018.
[24] Reist T, Koo D, Zingg D, Bochud P, Castonguay P, Leblond D. Cross-validation of high-fidelity aerodynamic shape optimization methodologies for aircraft wing-body optimization. AIAA J 2020;6:2581–95.
[25] Mura G, Hinchliffe B, Qin N, Brezillon J. Nonconsistent mesh movement and sensitivity calculation on adjoint aerodynamic optimization. AIAA J 2018;56(4):1541–53.
[26] Lea D, Allen M, Haine T. Sensitivity analysis of the climate of a chaotic system. Tellus A 2000;52(5):523–32.
[27] Wang Q, Gao J. The drag-adjoint field of a circular cylinder wake at reynolds numbers 20, 100 and 500. J Fluid Mech 2013;730:145–61.
[28] Wang Q. Convergence of the least squares shadowing method for computing derivative of ergodic averages. SIAM J Numer Anal 2014;52:156–70.
[29] Wang Q, Hu R, Blonigan P. Least squares shadowing sensitivity analysis of chaotic limit cycle oscillations. J Comput Phys 2014;267:210–24.
[30] Meyer K, Sell G. An analytic proof of the shadowing lemma. Funkcialaj Ekvacioj 1987;30:127–33.
[31] Pilyugin S. Shadowing in dynamical systems. Lecture Notes in Mathematics; 1999.
[32] Ni A, Wang Q. Sensitivity analysis on chaotic dynamical system by non-intrusive least square shadowing (NILSS). J Comput Phys 2017;347:56–77.
[33] Blonigan P, Murman S, Towne A. Reducing the cost of shadowing-based adjoint sensitivity analysis for turbulent flows. Center Turbul Res 2018.Proceedings of the Summer Program 2018
[34] Ni A, Murman S, Talnikar C. Adjoint sensitivity analysis on chaotic dynamical systems by non-intrusive least squares adjoint shadowing (NILSAS). J Comput Phys 2019;395:690–709.
[35] Dwight R, Brezillon J. Effect of various approximations of the discrete adjoint on gradient-based optimization. AIAA J 2006.2006–0690
[36] Zymaris A, Papadimitriou D, Giannakoglou K, Othmer C. Continuous adjoint approach to the spalart-allmaras turbulence model for incompressible flows. Comput Fluids 2009;38:1528–38.
[37] Hayek M, Wang Q, Laskowski G. Adjoint-based optimization of rans eddy viscosity model for u-bend channel flow. 2018 AIAA Aerospace Sci Meeting 2018:AIAA2018–2091.
[38] Verstraete T, Coletti F, Bulle J, Vanderwielen T, Arts T. Optimization of a u-bend for minimal pressure loss in internal cooling channels - part i: numerical method. J Turbomach 2013;135:051015.

[39] Coletti F, Verstraete T, Vanderwielen T, Bulle J, Arts T. Optimization of a u-bend for minimal pressure loss in internal cooling channels - part ii: experimental validation. J Turbomach 2013;135:051016.
[40] Alessi G, Verstraete T, Koloszar L, van Beeck J. Comparison of LES and RANS evaluations with experimental tests on u-bend duct geometry. Proc Inst Mech Eng, Part A 2020;234(3):315–22.
[41] Han J, Dutta S, Ekkad S. Gas turbine heat transfer and cooling technology. New York: Taylor and Francis; 2000.
[42] Elsayed K, Miranda J, Lacor C. Minimization of the pressure loss in internal cooling channels using the adjoint method. 1st Aviation Engineering Innovations Conference paper 2015:AEIC–2015–000.
[43] Zehner S, Steinbruck H, Neumann S, Weigand B. The ice formation method: a natural approach to optimize turbomachinery components. Int J Des Nature 2009;3 (4):259–72.
[44] He P, Mader C, Martin J, Maki K. Aerothermal optimization of a ribbed u-bend cooling channel using the adjoint method. Int J Heat Mass Transf 2019;140: 152–72.
[45] Namgoong H, Ireland P, Son C. Optimisation of a 180° u-shaped bend shape for a turbine blade cooling passage leading to a pressure loss coefficient of approximately 0.6. Proc Inst Mech Eng Part G 2016;230(8):1371–84.
[46] OpenFOAM, OpenFOAM.
[47] V. Supercomputer Centrum, VSC.
[48] Othmer C. A continuous adjoint formulation for the computation of topological and surface sensitivities of ducted flows. Int J Numer Methods Fluids 2008;58:861–77.
[49] Hinterberger C, Olesen M. Industrial application of continuous adjoint flow solvers for the optimization of automotive exhaust systems. ECCOMAS Thematic Conf CFD Opt 2011.2011–069
[50] Nocedal J, Wright S. Numerical optimization. Springer Science & Business Media; 2006.
[51] Gauger N, Ozkaya E. Single-step one-shot aerodynamic shape optimization. Int Ser Numer Math 2009;158:191–204.
[52] Alessi G, Koloszar L, Verstraete T, van Beeck J. Node-based adjoint surface optimization of u-bend duct for pressure loss reduction. Evolutionary and Deterministic Methods for Design Optimization and Control With Applications to Industrial and Societal Problems Computational Methods in Applied Sciences 2018;49:61–75.
[53] Taubin G. Curve and surface smoothing without shrinkage. Proc Fifth Int Conf Comput Vis 1995:852–7.